Impact of capillary pressure hysteresis and injection-withdrawal schemes on performance of underground hydrogen storage

Nazari, Farzaneh; Aghabozorgi Nafchi, Shokoufeh; Vahabzadeh Asbaghi, Ehsan; Farajzadeh, Rouhi; Niasar, Vahid J.

DOI
10.1016/j.ijhydene.2023.09.136

Publication date
2023

Document Version
Final published version

Published in
International Journal of Hydrogen Energy

Available online at www.sciencedirect.com

ScienceDirect

journal homepage: www.elsevier.com/locate/he

Impact of capillary pressure hysteresis and injection-withdrawal schemes on performance of underground hydrogen storage

Farzaneh Nazari [a], *Shokoufeh Aghabozorgi Nafchi* [b], *Ehsan Vahabzadeh Asbaghi* [a], *Rouhi Farajzadeh* [c,d], *Vahid J. Niasar* [a,*]

[a] *Department of Chemical Engineering, The University of Manchester, Oxford Road, Manchester, M13 9PL, UK*
[b] *Wood Group PLC, Aberdeen, Scotland, United Kingdom*
[c] *Faculty of Civil Engineering and Geosciences, Delft University of Technology, P.O. Box 5048, Delft, GA 2600, the Netherlands*
[d] *Shell Global Solutions International B.V., The Hague, the Netherlands*

HIGHLIGHTS

- Buoyancy plays a significant role on UHS performance.
- A dimensionless number analysis to study the influence of injection/withdrawal schemes on UHS performance.
- Capillary pressure scanning curves did not significantly affect the hydrogen saturation distribution.
- Water upconing limits the UHS performance at high flow rates.
- Interplay between Bond and capillary numbers should be considered for UHS.

GRAPHICAL ABSTRACT

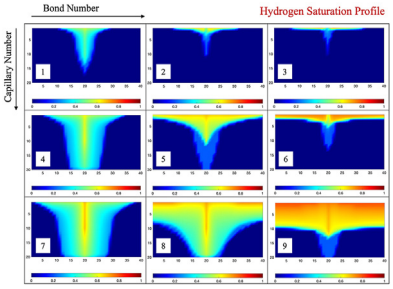

ARTICLE INFO

Article history:
Received 7 June 2023
Received in revised form
11 July 2023
Accepted 12 September 2023
Available online 04 October 2023

Keywords:
Capillary Pressure Hysteresis
Underground hydrogen Storage

ABSTRACT

Hypothesis: Underground hydrogen storage in depleted hydrocarbon reservoirs and aquifers has been proposed as a potential long-term solution to storing intermittently produced renewable electricity, as the subsurface formations provide secure and large storage space. Various phenomena can lead to hydrogen loss in subsurface systems with the key cause being the trapping especially during the withdrawal cycle. Capillary trapping, in particular, is strongly related to the hysteresis phenomena observed in the capillary pressure/saturation and relative-permeability/saturation curves. This paper address two key points: (1) the sole impact of hysteresis in capillary pressure on hydrogen trapping during withdrawal cycles and (2) the dependency of optimal operational parameters (injection/withdrawal

* *Corresponding author.*
E-mail address: vahid.niasar@manchester.ac.uk (V.J. Niasar).
https://doi.org/10.1016/j.ijhydene.2023.09.136

Scanning Curves
Numerical Simulation

flow rate) and the reservoir characteristics, such as permeability, thickness and wettability of the porous medium, on the remaining hydrogen saturation.

Model: To study the capillary hysteresis during underground hydrogen storage, Killough [1] model was implemented in the MRST toolbox [2]. A comparative study was performed to quantify the impact of changes in capillary pressure behaviour by including and excluding the hysteresis and scanning curves. Additionally, this study investigates the impact of injection/withdrawal rates and the aquifer permeability for various capillary and Bond numbers in a homogeneous system.

Findings: It was found that although the hydrogen storage efficiency is not considerably impacted by the inclusion of the capillary-pressure scanning curves, the impact of capillary pressure on the well properties (withdrawal rate and pressure) can become significant. Higher injection and withdrawal rates does not necessarily lead to a better performance in terms of productivity. The productivity enhancement depends on the competition between gravitational, capillary and viscous forces. The observed water upconing at relatively high capillary numbers resulted in low hydrogen productivity. highlighting the importance of well design and placement.

1. Introduction

1.1. Underground hydrogen storage

The low-carbon energy industry requires a long-term solution to overcome the intermittent nature of the renewable energy sources and to provide year-round electricity. The cyclic intermittent nature of these resources leads to energy surplus during high energy production season and vice versa [3]. Moreover, heavy industries, such as steel mining, require high-temperature heat that cannot be easily supplied by electricity. The energy produced during a productive season can be stored for use during the shortage times. Additionally, this excess produced energy needs a durable and efficient storage medium able to hold it for different durations of time (days, months, or even years). Due to its desirable characteristics, H_2 is a favorable medium to/from which the excess low-carbon electricity can be converted [4,5] through electrolysers and fuel cells a [6,7], for instance Refs. [8–11], while it can accommodate the high-temperature requirements that heavy industries deal with. The successful implementation of hydrogen economy [5,7] requires proper storage spaces to hold the hydrogen itself. The produced H_2 can be stored in surface or subsurface structures. Hydrogen storage in high-pressure gas cylinders, and cryogenic tanks [12–14] can be some example cases of surface hydrogen storage. However, surface energy storage may not be a long-term solution as surface structures only provide limited storage capacities. Underground Hydrogen Storage (UHS), on the other hand, can become a viable solution enabling industries to have access to continuous energy supply as they provide safe storage spaces compared to the limited spaces that the surface structures provide. These subsurface structures may include aquifers [15–17], depleted oil and gas reservoirs [18], and salt caverns [19,20]. Subsurface hydrogen storage, although an intriguing option, comes with complexities that need to be assessed prior to the storage process. H_2 storage in salt caverns, for instance, is restricted by the limited volume that these structures offer. Depleted oil and gas reservoirs also contain significant amounts of trapped/residual hydrocarbons that can react with H_2 and also reveal relatively high levels of microbial activity that can lead to H_2 loss [21]. Aquifers, on the other hand, maybe a suitable alternative as they can provide vast storage spaces, and demonstrate less chance of microbial/chemical reactions [16,22].

1.2. Hysteresis and trapping

There are various hydromechanical processes that may cause hydrogen loss in UHS. Examples include loss of purity of hydrogen due to mixing with the cushion gas [23,24] or other in-situ gases [25], lateral spreading of hydrogen due to strong buoyancy [26,27], and ultimately trapping of hydrogen due to structural trapping, dissolution trapping, mineral trapping, and residual trapping, similar to CO_2 storage in aquifers [28]. It should also be noted that in CO_2 storage, the main objective is maximising the trapping efficiency, whereas in UHS, the aim is to minimise the trapping to decrease hydrogen loss, and therefore, a formation suitable for CO_2 storage might be unfit for UHS.

The residual trapping, in particular, is initiated by the wettability preference of the subsurface rocks. It is closely linked with the hysteresis phenomena, which shows the dependence of flow on its history. This path dependence can be studied in terms of contact angle, capillary pressure-saturation (P_c-S_w) and relative permeability-saturation (k_r-S_w) functions. Due to capillary trapping and hysteresis, the P_c-S_w and k_r-S_w functions will not be unique and will differ for drainage and imbibition processes [29–31]. This behaviour can be enhanced during the UHS because of its cyclic nature and also the strong water wetting conditions [32].

A complete hysteresis analysis can be done through scanning curves to consider the full hysteresis cycles of P_c-S_w

and k_r-S_w. Depending on the initial condition and two-phase flow process, P_c-S_w and k_r-S_w will follow one of the primary drainage, main drainage, primary imbibition, or imbibition curves (these are called bounding curves) until they reach a turning point due to the reversal in flow path. From that point, a new scanning curve would be formed, which is bounded by the main drainage-imbibition curves. The formation of the scanning curves from a previous one continues as long as the reversals occur. Different models have been suggested to generate the scanning curves from the bounding drainage/imbibition curves and characterize trapping. Avid reader is referred to literature for a detailed study of such models [1,32–41].

The CO_2 capillary trapping has proven to happen significantly in underground storage sites, which is a favorable process in CCS as opposed to hydrogen capillary trapping in UHS [42,43]. Akbarabadi and Piri [42] observed high capillary-trapping efficiency, particularly for gaseous CO_2 [42] in their experiments. Juanes et al. [31] employed the Killough [1] and Land [35] models to investigate the impact of relative-permeability hysteresis and the non-wetting phase trapping in the context of CO_2 sequestration. However, they ignored the effect of capillary-pressure hysteresis on the flow properties [31,44]. Ide et al. [45] investigated the effect of dimensionless gravity number, aquifer inclination, and capillarity on the amount of trapped CO_2, and concluded that as the gravity number increases, the amount of the trapped gas decreases, although the aquifer inclination showed the opposite trend [45]. Gershenzon et al. [46] used Killough [1] k_r-S_w model to study the CO_2 trapping in terms of snap-off and capillary pinning using ECLIPSE-300 [46–49], however, they ignored the capillary-pressure hysteresis.

To investigate the impact of aquifer heterogeneity on the capillary trapping of CO_2, Yang et al. [50] employed an invasion percolation model combined with Land [35] and Spiteri et al. [37] trapping models. Wang et al. [30] investigated the solubility and residual trapping of CO_2 during full-cycle injections, employing the Killough [1] P_c-S_w and k_r-S_w model to generate the first scanning curves; however, they did not consider all possible cycles and scanning curves due to hysteresis in the system. To examine the importance of the gas/liquid relative-permeability hysteresis on the UHS, Bo et al. [17] employed the experimentally-measured data of Boon and Hajibeygi [51] along with the GEM simulator [52]. Their results indicate that hysteresis effect in gas and liquid flows gain importance at differing injection/withdrawal rates. Moreover, they emphasized the importance of considering the measured k_r-S_w hysteresis data for the H_2-water fluids, as it highly influences the H_2 productivity estimation. In another study, Pan et al. [16] examined the impact of relative-permeability hysteresis, wettability, and injection/withdrawal scenarios during UHS, and compared the performance of CO_2-brine systems with H_2-brine systems. They showed that the inclusion of hysteresis in H_2-brine relative permeability lowers the H_2 productivity in terms of withdrawal efficiency [16]. Lysyy et al. [53] used the experimentally-measured H_2-brine k_r values [54] to investigate the impact of hysteresis in k_r data on H_2 storage. The findings demonstrated that the ultimate recovery factor was overestimated by nonhysteretic k_r values.

1.3. The present study

There is limited information in the literature regarding the sole influence of capillary-pressure hysteresis on UHS performance as most studies only include the relative-permeability hysteresis. Clearly, in Darcy's law, relative permeability and its hysteresis directly control the two-phase flow dynamics and trapped saturation. As hysteresis calculations are computationally expensive and time consuming, here, we seek to explore the hysteresis in capillary pressure to determine if it presents a substantial impact on the flow characteristics and efficiency and to see whether we can exclude its effect to increase the calculation speed. Therefore, we will investigate the impact of hysteresis in P_c-S_w curves and trapping during cyclic H_2 injection and withdrawal by taking into account the full scanning behaviour in each individual grid block of the model during drainage and imbibition processes, while ignoring the hysteresis in relative permeability. Moreover, we investigate the impact of flow rates, on the UHS efficiency. In summary, this study provides the following key contributions by applying the Killough [1] model for hysteresis in capillary pressure and MRST toolbox [2,55].

- Investigating the impact of P_c-S_w curves on H_2 loss due to trapping and saturation distribution in aquifers.
- Performing a comparative study to quantify the impact of including and ignoring P_c-S_w curves and their hysteresis on the amount of trapped H_2 and saturation distribution after injection/withdrawal cycles,
- Probing the impact of dimensionless numbers, namely capillary, Bond, and buoyancy numbers (as the ratios of viscous, capillary and gravitational forces) on H_2 injection/withdrawal cycles.
- Discussing the relevance of water upconing on H_2 production efficiency.

The remainder of this paper first presents a summary of the methodology and tools used for generating the bounding/scanning P_c-S_w curves and modeling the H_2 injection/withdrawal cycles. Next, we will present the results regarding the impact of intermediate P_c-S_w scanning curves as well as the influence of the viscous/buoyancy forces on the H_2 storage efficiency. Finally, a discussion on the numerical instability for hysteresis modeling and the complexities will be provided.

2. Methodology

2.1. The Main Capillary Pressure - Saturation Curves

It has been shown in the literature that H_2 and N_2 exhibit similar (flow) characteristics in porous media, for example in terms of three-phase contact angle [56], because the three-phase systems containing these gases (gas-brine-rock) present similar van der Waals and electrostatic interactions. Therefore, the N_2-water P_c-S_w data from Plug and Bruining [57] is used as the initial input for calculating H_2-water P_c-S_w curve. The data is scaled using the Leverett J-function $J(S_w) = \frac{P_c(S_w)\sqrt{K/\varphi}}{\sigma\cos\theta}$ [58] to account for the impact of permeability.

Afterwards, the Brooks-Corey [59] formulation (equation (1)) is used to fit the scaled P_c-S_w curves:

$$P_c(S_w) = P_e \times S_w^{*\,n} \tag{1}$$

where P_e is the entry capillary pressure, S_w^* is the scaled wetting phase saturation ($S_w^* = \frac{S_w - S_{rw}}{1 - S_{rw} - S_{rnw}}$), S_{rw} and S_{rnw} are the residual saturations of the wetting (water) and non-wetting (hydrogen) phases, respectively. The relative-permeability values are also calculated using the Brooks-Corey equations [59], where $k_{r\alpha}^{max}$ denotes the endpoint relative permeability for each phase:

$$k_{r\alpha}(S_\alpha) = k_{r\alpha}^{max} \times S_\alpha^{*\,m} \tag{2}$$

2.2. The Scanning Capillary Pressure - Saturation Curves

The P_c along the scanning curve is computed using Equation (1), considering a secondary imbibition process starting from the main drainage curve (Equation (3)). In this equation, P_c^{Dr} and P_c^{Im} show the main drainage and imbibition curves, S_w^{Hyst} is the turning point wetting-phase saturation, S_w^{Max} denotes the maximum attainable wetting-phase saturation, and ϵ is a curvature parameter [1] (See Fig. 1b for an example of scanning curves generated by this model).

$$P_c^{Sc}(S_w) = P_c^{Dr}(S_w) - F \times \left[P_c^{Dr}(S_w) - P_c^{Im}(S_w)\right]$$
$$F = \frac{\frac{1}{S_w - S_w^{Hyst} + \epsilon} - \frac{1}{\epsilon}}{\frac{1}{S_w^{Max} - S_w^{Hyst} + \epsilon} - \frac{1}{\epsilon}} \tag{3}$$

The secondary scanning P_c-S_w curves starting from a prior scanning curve (other than the main curves) can also be calculated using the methodology outlined in Killough [1] and Guo [60]. The generation of the n-th scanning curves requires the turning point history of the grid blocks as well as their P_c-S_w functions. For instance, to generate the n-th drainage scanning curve (initiated from an imbibition scanning curve), one can follow Equations (4)–(6) as outlined by Guo [60]. In these equations, S_{w1} and S_{w2} are imbibition-to-drainage and previous drainage-to-imbibition turn-around saturations, respectively, and P_c^{Sc} is the capillary pressure on the scanning curve. Similar formulations are also applied for the scanning imbibition-to-drainage processes and can be found in Guo [60] and Killough [1].

$$P_c^{Sc} = P_c^{Im}(S_w) + \left[\frac{\frac{1}{\Delta S_w^{Hyst} + \epsilon} - \frac{1}{\epsilon}}{\frac{1}{\Delta S_w + \epsilon} - \frac{1}{\epsilon}}\right]\left[P_c^{Dr}(S_w) - P_c^{Im}(S_w)\right] + (\delta P_1 - \delta P_2) \tag{4}$$

where:

$$\delta P_1 = \left[P_c^{Sc}(S_{w1}) - P_c^{Im}(S_{w1})\right]\frac{\Delta S_{w2}^{Hyst}}{\Delta S_w}$$
$$\delta P_2 = \left[P_c^{Dr}(S_{w2}) - P_c^{Sc}(S_{w2})\right]\frac{\Delta S_{w1}^{Hyst}}{\Delta S_w} \tag{5}$$

and:

$$\Delta S_{w1}^{Hyst} = S_{w1} - S_w \quad , \quad \Delta S_{w2}^{Hyst} = S_w - S_{w2} \quad \text{and} \quad \Delta S_w = S_{w1} - S_{w2} \tag{6}$$

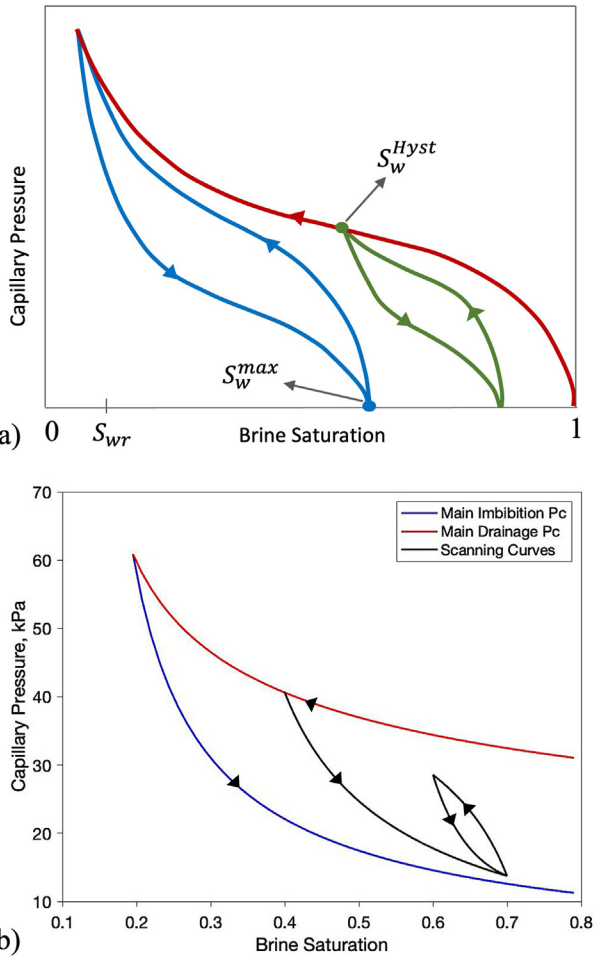

Fig. 1 – (a) Schematic of the capillary-pressure hysteresis and the scanning curves. The red, blue, and green curves illustrate the primary drainage, the main hysteresis loop, and a scanning loop generated at a different turning point saturation (reproduced from Joekar-Niasar et al. [29]). S_w^{Hyst} denotes the turning-point saturation of the non-wetting phase and S_w^{max} is the maximum attainable wetting phase saturation. (b) An example of the scanning P_c-S_w curves generated using the Killough [1] model based on the main Brooks-Corey capillary-pressure model. (For interpretation of the references to color in this figure legend, the reader is referred to the Web version of this article.)

Note that the application of any generated scanning curve from another scanning curve is only valid in the saturation range of the two consecutive turning points ($S_{w2} < S_w < S_{w1}$). For saturations outside of this range, the scanning curve continues on the capillary-pressure curve generated at time-step t^{i-2}, where i is an index indicating the current timestep number. A diagram of the P_c scanning behaviour is shown in Fig. 1a, where depending on the saturation at the turning point, various scanning curves can be produced [29]. Fig. 1b also represents a real scanning curve analysis generated based on the Killough [1] model. It can be seen that depending on the saturation of the turning point, the scanning curves may/may not reach the main P_c-S_w curves.

In a multi-phase system, capillary forces are only one factor influencing flow efficiency; other density/viscosity-driven forces also impose major impacts on flow behaviour and productivity. Viscous and buoyancy forces, in particular, gain tremendous importance as the H_2-brine system present large viscosity and density differences. Thus, it is vital to quantify impact of these forces, which will be done through a dimensionless number analysis by considering three numbers, namely capillary number (*Ca*) [58], Bond Number (*Bo*), and Buoyancy Number (*Bu*) [61,62]. *Ca* is defined as the ratio of viscous to capillary forces, *Bo* signifies the ratio of gravitational to capillary forces. Based on these two numbers, *Bu* number is proposed as the ratio of gravitational to viscous forces, which is less commonly used. The following definitions are used to calculate these numbers, respectively, where μ_g, q_g, σ, and φ represent the gas viscosity, injection/withdrawal Darcy velocity, interfacial tension, and aquifer porosity, respectively. K_v and r also represent the aquifer permeability (in the vertical direction) and characteristic pore radius, in turn.

$$Ca = \frac{\mu_g q_g}{\sigma\varphi\cos\theta} \quad , \quad Bo = \frac{\Delta\rho g h K_v}{\sigma r} \quad , \quad \text{and} \quad Bu = \frac{\Delta\rho g h K_v \varphi\cos\theta}{\mu_g q_g r} \tag{7}$$

2.3. Model implementation

As previously demonstrated, a complete P_c-S_w hysteresis study was performed by considering all the predictable scanning curves that the simulation grid blocks can follow. The main steps for conducting the P_c-S_w hysteretic behaviour are presented in Fig. 2. To this end, the saturations at three consecutive time steps are used to determine whether a grid block will continue to drain, imbibe, or will have a turning point. Note that the local grid imbibition/drainage cycles are independent of the main injection/withdrawal schemes, meaning some grid blocks can go through an imbibition process while the main operation is controlled by the injection of the non-wetting phase (drainage). If a grid block demonstrates a reversal in its saturation trend, the Killough [1] model will be used to generate a new P_c-S_w function based on the turning point saturation value, otherwise, the P_c functions would stay the same as the previous timestep. This procedure will be repeated at every time step for all the grid blocks to determine the local grid processes and their corresponding P_c-S_w functions.

We have implemented the mentioned P_c-S_w hysteresis model in the MATLAB Reservoir Simulation Toolbox (MRST) [2,55], which is used for simulating the H_2 injection/withdrawal. In particular, we used the object-oriented, automatic-differentiation (AD-OO) framework in MRST employing a fully-implicit scheme to calculate pressure and saturation simultaneously.

3. Results and discussion

3.1. Input parameters

The parameters outlined in Table 1 are used as the input to the aforementioned P_c-S_w hysteresis model. It should be noted that the impact of fluid and rock compressibilities has been neglected in this study. To elaborate on the potential importance of hydrogen compressibility, we conducted two simulations using a single injection scenario assuming

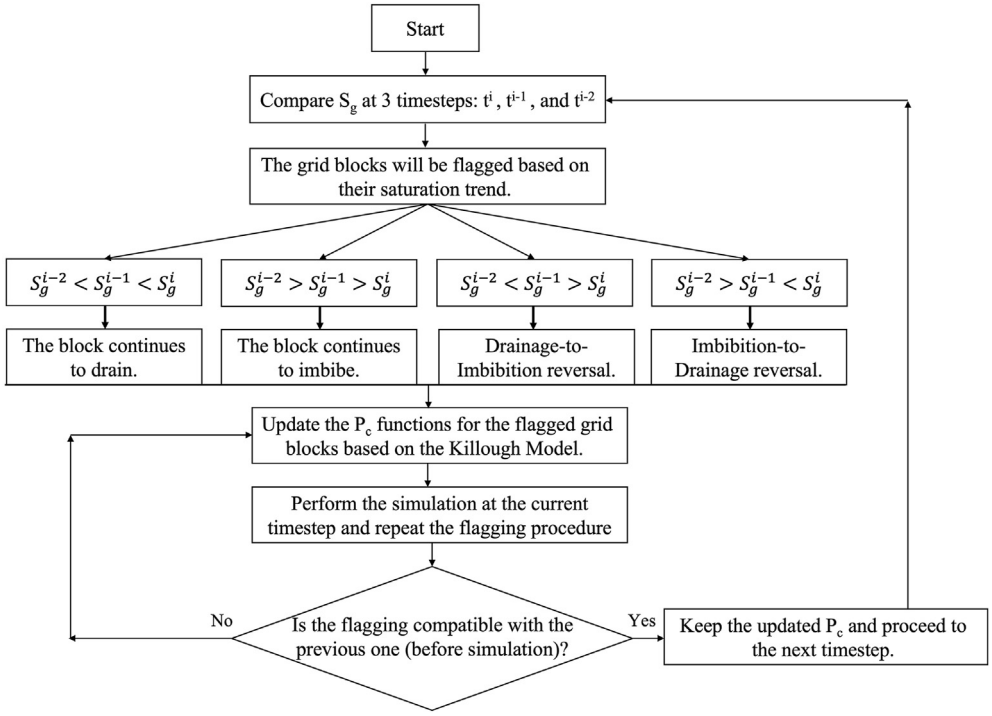

Fig. 2 – A diagram outlining the steps taken to simulate the injection and withdrawal of H_2 using scanning analysis.

Table 1 – A summary of basic parameters used in the model.

Parameter	Value
Permeability, mD	250 [2]
Porosity, (–)	0.25 [2]
Aquifer Depth, m	1500
Aquifer Thickness, m	100
Aquifer Lateral Size, m	1000
Brine Density, kg/m^3	1000 [63]
Brine Viscosity, cp	0.80 [63]
H_2 Density, kg/m^3	15[a]
H_2 Viscosity, cp	0.01 [64]
Interfacial Tension, mN/m	72 [65,66]
Reference Pressure, MPa	15 [2]

[a] Calculated based on the ideal gas law (Compressibility factor = 1).

Table 2 – Petrophysical properties used in the model. The P_c data are derived by consecutive scaling [58] and Brooks-Corey [59,67] fitting of Nitrogen data presented in Plug and Bruining [57].

Parameter	Value
Corey Exponent for Water k_r function	4
End point k_r value for Water	0.40
Corey Exponent for H_2 k_r function	2
End point for H_2 k_r value	0.80
Corey Exponent for Drainage P_c function	0.31
Entry P_c value for Drainage, kPa	31
Corey Exponent for Imbibition P_c function	0.77
Entry P_c value for Imbibition, kPa	11
Irreducible Water Saturation	0.12 [2]
Residual Gas Saturation	0.21 [2]

compressible and incompressible gases. Note that the compressible simulation has been done using the constant gas compressibility assumption. For comparison, the hydrogen saturation fronts were plotted as a function of aquifer depth and length as shown in Figure Appendix C.1. It can be seen that the two cases present small differences, especially near the well. However at very long injections when full segregation takes place, there is a considerable difference in fronts. Given the cyclic injection - withdrawal of hydrogen at much smaller PVs and to reduce further complexities in the model, we have neglected the impact of fluid compressibility in the simulations. Table 2 shows the petrophysical properties used in conjunction with the Brooks-Corey k_r-S_w and P_c-S_w formulations. As mentioned, we used N_2-water P_c-S_w data [57] and scaled it for the H_2-water system. The entry capillary pressure and exponents demonstrate the Brooks-Corey [59] fitted values after scaling. The data presented by Plug and Bruining [57] is shown in Fig. 4 as well. The aquifer is also considered to be fully water wet ($\cos\theta = 1$). Fig. 3 shows the simulation domain, initial conditions, and boundary conditions. We have considered a 1000 × 1000 × 100 m^3 homogeneous aquifer with its bottom border regarded as an open flow boundary, while the vertical boundaries are designated as no-flow boundaries. The injection/withdrawal well is perforated down to half of the aquifer thickness and is placed in the middle of X–Y plane. A sensitivity analysis was performed to check the impact of the grid resolution on the results, which is presented in Appendix A.

The H_2 injection/withdrawal schemes considered in this study include two consecutive cycles of injection-withdrawal in a fully water-saturated aquifer. Note that the injection/

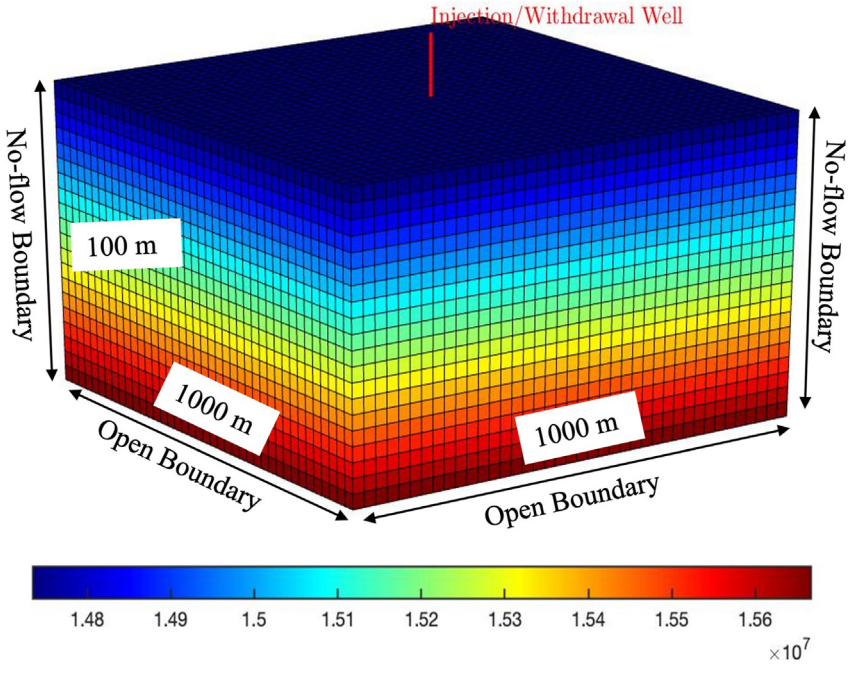

Fig. 3 – The simulation domain and initial pressure conditions of the aquifer in Pa. Hydrostatic initial pressure condition has been assumed, all boundary faces are closed (no flow), except the bottom boundary, which is open flow. The injection/withdrawal well is considered at the centre of the aquifer and has penetrated the aquifer to its half depth.

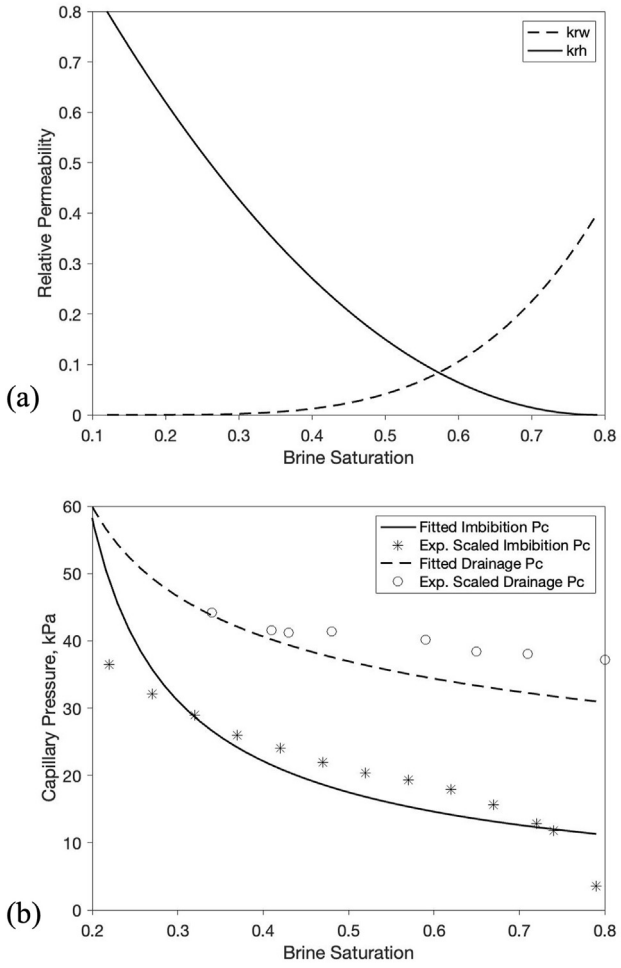

Fig. 4 – (a) The H_2 (k_{rh}-S_w) and water (k_{rw}-S_w) relative permeability curves used in this study. The k_r-S_w values are calculated according to Brooks-Corey Equation [59]. The Corey exponents for H_2 and water are 2 and 4, respectively. The endpoint relative permeability values for water and H_2 are set equal 0.4 and 0.8, respectively. (b) The imbibition and drainage P_c-S_w data used in this study, fitted by the Brooks-Corey equation [59]. The Corey exponents for imbibition and drainage are equal 0.77 and 0.31, respectively. The entry capillary pressure values are also set equal 11 and 31 kPa. To derive this data first the N_2 data of Plug and Bruining [57] were scaled using the Leverett J-Function [58], then the capillary pressure values was fitted to the Brooks-Corey equation.

withdrawal rates are kept constant for each simulation case. The first injection phase continues for 6 months, followed by 3-month withdrawal-injection-withdrawal phases.

The remaining of this paper is devoted to how the hysteresis in P_c-S_w curves affects the UHS. The impact of the flow rate and aquifer characteristics will be examined by running the simulations for various *Ca* and *Bo* numbers. The last section will also include a discussion on the numerical complexities that may be encountered using the scanning curves.

3.2. *Capillary pressure - saturation hysteresis*

This first modeling case probes the effect of P_c-S_w hysteresis on the efficiency of the H_2 injection/withdrawal cycles when considering a low capillary number ($Ca = 2 \times 10^{-7}$) equivalent to 0.01 PV/year (684 m^3/day) and $Bo = 0.44$. H_2 injection/withdrawal is regarded to happen in two cycles, with the first injection lasting six months, and the subsequent withdrawal, injection, withdrawal each for three months.

For comparison of the impact of P_c-S_w hysteresis, the cyclic simulations were repeated for four cases: 1) P_c-S_w hysteresis with full scanning behaviour, 2) P_c-S_w hysteresis only with main loops (no scanning), 3) drainage P_c-S_w curve with no hysteresis, and 4) zero capillary pressure. Fig. 5 shows the H_2 saturation profile at the end of the second injection and withdrawal when the P_c-S_w scanning curves were included. Table 3 details the difference between the four scenario cases in terms of produced H_2 volume and remained H_2 saturation in the aquifer. It can be concluded that assumptions related to ignoring the hysteresis or ignoring the capillary pressure (Scenarios 2–4) slightly underestimate remaining H_2 saturation for this specific case. However, due to the competition between viscous, capillary, and gravitational forces, this underestimation may be pronounced under different conditions. Figure Appendix B.1 also presents the data regarding the H_2 operational flow rate and bottom-hole pressure as a function of time for these four cases. It can be seen that the P_c mainly influences the bottom-hole pressure and flow rate at late-time withdrawal, when the H_2 withdrawal rate is fallen as a result of water production. Moreover, during the second withdrawal stage, the bottom-hole pressure has fallen less noticeably for the scanning (first) scenario compared to second and third scenarios. Moreover, it can be deducted that the flow rate will be overestimated when neglecting the P_c effect. It can be concluded that although the impact of P_c scenarios is not significant in terms of saturation distribution and remaining saturation, their influence on the pressure field and well properties, especially at late-time, can become noticeable.

3.3. *Dimensionless number analysis*

The interaction of viscous, capillary, and gravitational forces determines how efficiently a UHS design operates. The relative significance of these forces can be quantified using the dimensionless capillary, Bond, and buoyancy numbers as defined in Equation (7). Capillary number, for instance, is directly connected to injection/withdrawal rates, which its optimization is vital for a successful and low-loss UHS operation. In this section, impact of variations of these dimensionless numbers on H_2 removal has been investigated. To determine how effective certain scenarios are, we set a withdrawal cut-off constraint equal to 10% gas-cut (Q_g/Q_{total} >

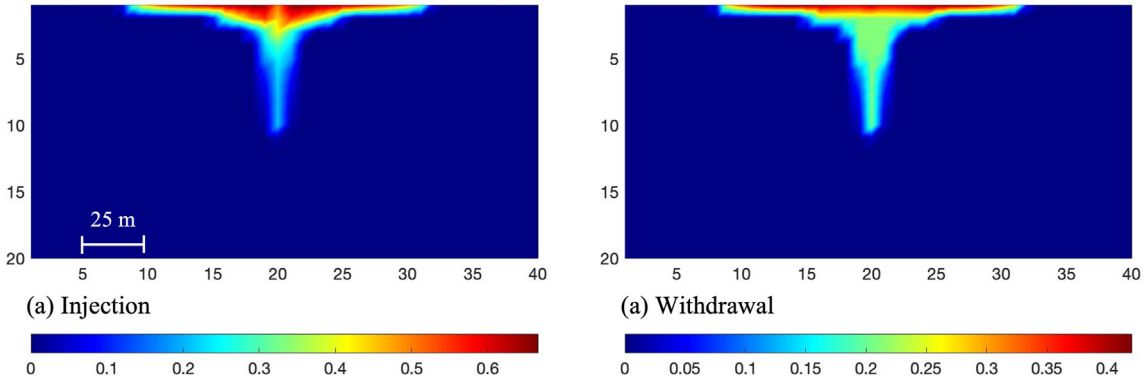

Fig. 5 – H_2 saturation profile at the end of (a) second injection and (b) second withdrawal with including P_c-S_w scanning curves (first case in Table 3) for $Ca = 2 \times 10^{-7}$ and $Bo = 0.44$. Given the slow viscous force and intermediate Bond numbers, hydrogen saturation override is significant.

Table 3 – A quantitative comparison between four cases with different P_c models. For these scenarios, no cut-off constraint is applied, and the second withdrawal time is set to three months. The injection/withdrawal rate is equal to 0.01 PV/year and $Ca = 2 \times 10^{-7}$. The error value is calculated considering the first scenario as the base case ($(|S^i_{g,rem} - S^1_{g,rem}| / S^1_{g,rem})$). The total injected pore volume is equal to 0.009.

Case Number	Description	Produced H_2 Pore Volume	Remaining H_2 Saturation	Remaining H_2 Relative Difference, %
1	Hysteresis in P_c-S_w curves - with scanning curves	4.638×10^{-3}	0.276	–
2	Hysteresis in P_c-S_w curves - bounding curves only	4.622×10^{-3}	0.269	−2.460
3	No hysteresis - only drainage P_c-S_w	4.642×10^{-3}	0.268	−2.858
4	No capillary pressure	4.778×10^{-3}	0.272	−1.483

Table 4 – A quantitative comparison between nine cases of H_2 injection/withdrawals indicating the significance of Capillary, Bond, and Buoyancy numbers on the H_2 productivity. The second withdrawal stops when the gas-cut reaches 10%. The remaining H_2 saturations quantifies the average saturation of grid blocks containing $S_g > 0.05$. The H_2 saturation profiles regarding these cases are shown in Figs. 7 and 8.

Case Number	Injected PV, 1/year	Capillary Number, (–)	Bond Number, (–)	Buoyancy Number, (–)	Produced Pore Volume	Remained H_2 Saturation	Withdrawal Time, Days
1	0.01	2×10^{-7}	0.13	6.5×10^{5}	5.00×10^{-3}	0.21	97.25
2	0.01	2×10^{-7}	0.44	2.20×10^{6}	5.44×10^{-3}	0.25	210.01
3	0.01	2×10^{-7}	0.88	4.40×10^{6}	4.40×10^{-3}	0.28	289.91
4	0.13	2×10^{-6}	0.13	6.50×10^{4}	2.95×10^{-2}	0.21	46.11
5	0.13	2×10^{-6}	0.44	2.20×10^{5}	5.64×10^{-2}	0.28	148.84
6	0.13	2×10^{-6}	0.88	4.40×10^{5}	5.64×10^{-2}	0.34	208.19
7	0.63	1×10^{-5}	0.13	1.30×10^{4}	6.52×10^{-2}	0.21	20.54
8	0.63	1×10^{-5}	0.44	4.40×10^{4}	2.49×10^{-1}	0.25	123.73
9	0.63	1×10^{-5}	0.88	8.80×10^{4}	3.53×10^{-1}	0.24	166.18

0.1) during the second H_2 withdrawal phase. For simulations, P_c-S_w hysteresis without the scanning curves were considered (case 2 in Table 3), as inclusion of the scanning curves in MRST led to significantly higher computational cost. To elaborate, the variations in the capillary number and Buoyancy number can be achieved by changing the flow rates. Altering the aquifer permeability, which would directly affect the P_c-S_w functions, is another way to examine the effect of Bond and Buoyancy numbers. In order to do this, three different permeability scenarios (50, 250, and 1000 mD) and three injection/withdrawal rates were considered, which resulted in nine cases. The average pore radius to calculate the Bond numbers were taken from the study of Kashif et al. [68]. A summary of these cases is presented in Table 4 and Fig. 6 with the visualisation displayed in Figs. 7 and 8 showing Y-Z aquifer slices where the injection/withdrawal happens.

Considering the variations in capillary number, it can be seen that the withdrawal constraint is satisfied earlier when the capillary number rises (flow rate increases), and the H_2 removal would be halted due to the high water withdrawal. As Pan et al. [16] also mentioned, larger withdrawal rates cause the reservoir pressure to drop more noticeably, therefore it is

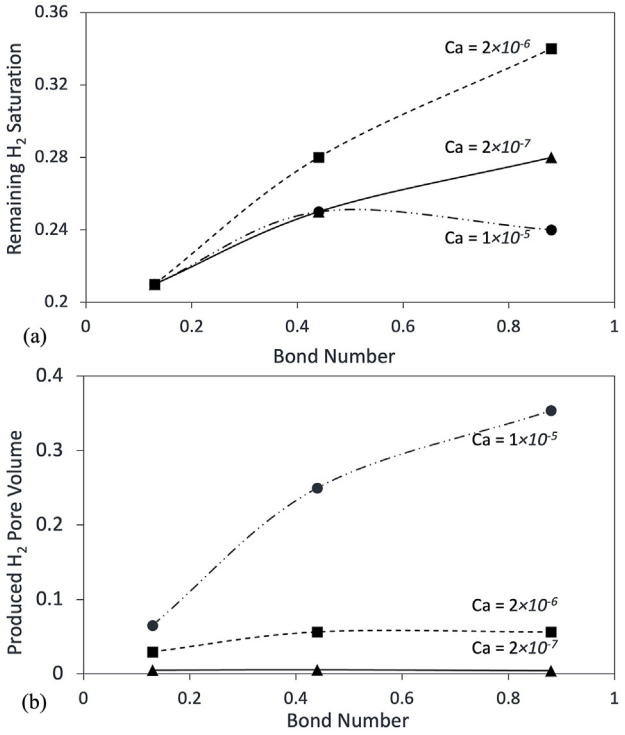

Fig. 6 – Impact of Bond number and capillary number on (a) remaining H_2, (b) produced H_2 in pore volume. All plotted results are related to the end of second withdrawal for the nine cases presented in Table 4. The second withdrawal stops when the gas-cut reaches 10%. The remaining H_2 saturations quantifies the average saturation of grid blocks containing $S_g > 0.05$. The H_2 saturation profiles regarding these cases are shown in Figs. 7 and 8.

critical to maintain the aquifer pressure by injecting a large initial H_2 volume or other cushion gases. Variation of the pressure and flow rate versus time for some cases is shown in Figure Appendix B.2. Higher H_2 removal rates can be attained when the aquifer pressure is maintained because viscous forces predominate and reduce H_2 lateral spreading [16]. However, caution must be taken while increasing the capillary number since at high flow rates, the magnitude of viscous forces increases and therefore, water upconing would be unavoidable and would stop the withdrawal of H_2. A graphical representation of water upconing during the second H_2 withdrawal at a rate of 0.13 PV/year ($Ca = 2 \times 10^{-6}$, $Bo = 0.44$) is shown in Fig. 9. The graph shows the H_2 saturation at six different timesteps, from the second withdrawal up until the water upconing is fully formed. When upconing takes place, water bypasses H_2 and will breakthrough to the withdrawal well faster, trapping the H_2 in the aquifer.

The relative magnitude of gravitational forces compared to capillary forces can be investigated using the dimensionless Bond number. In order to consider the effect of variations in aquifer permeability on capillary pressure curves, we have used the Leverett J-Fuction $J(S_w) = \frac{P_c(S_w)\sqrt{K/\varphi}}{\sigma \cos\theta}$ [58] to re-scale the P_c-S_w curves. At a constant capillary number, as shown in Table 4 and Figs. 6–8, when the Bond number drops (permeability reduces), the interfaces become more diffuse and H_2 finds it more difficult to travel upwards, which causes it to spread out more in the aquifer. As a result, at low Bond numbers, as contrasted to high Bond numbers (high permeability values), the cut-off requirement is satisfied significantly earlier. Although higher vertical aquifer permeability appears to be beneficial for H_2 removal, caution should be used when selecting a UHS site. Higher horizontal aquifer permeability results in faster lateral spreading of H_2, which allows H_2 to escape through the aquifer's spill points. Another important implication is that although an increase in capillary number results in reduced withdrawal time, according to Fig. 6a, there is non-monotonic trend between remaining H_2 and Bond number at high capillary numbers. This means that at a certain range of Bond number values, it is even more beneficial to increase the operational flow rate as the trapped saturation would decrease. This also enhances the significant impact of aquifer permeability on the UHS design.

3.4. *Discussion on numerical challenges*

As previously noted, we have simulated the H_2 injections and withdrawals as well as the hysteresis behaviour using the MRST toolbox [2,55]. Killough [1] methodology was used to implement the P_c model in the MRST AD-OO solver to create the scanning curves. However, there are a few issues that needs to be discussed and clarified because they have a significant impact on the simulation operation for including scanning curves.

The complexities can be first discussed regarding the Killough [1] methodology. The turning point history of the grid blocks, the relative placement of the turning points to one another, and the gas saturation at those turning points are all important factors in achieving appropriate, bounded scanning curves from the model, especially when grid blocks go through subsequent drainage and imbibition phases and present a high number of turning points. Not-bounded scanning curves may be achieved depending on the occurrence of the stated factors, which needs to be handled. The new scanning curves can also only be generated between the saturation range of two subsequent turning points. The model must be able to manage saturation values outside of this range by re-calling the P_c-S_w curve at timestep t^{i-2} (either the scanning or main curve depending on the number of turning points).

On the other hand, the inclusion of the P_c-S_w scanning model presented a high level of complexity by significantly increasing the number of timesteps needed as well as the time required for solving each timestep. Additionally, these

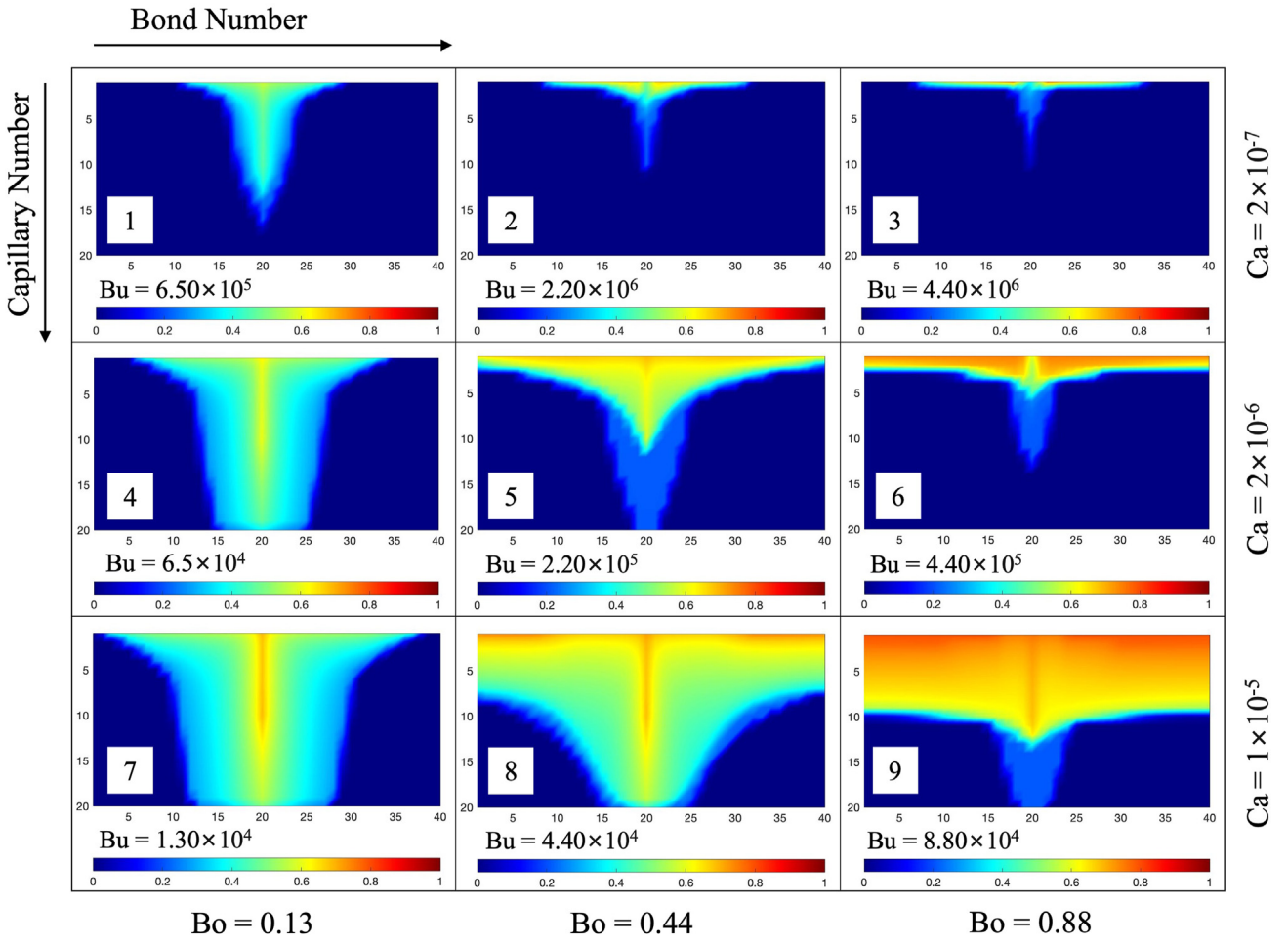

Fig. 7 – Visualisation of hydrogen plume at different capillary, Bond, and Buoyancy numbers at the end of the second injection. Each row presents 3 cases at a constant capillary number. The quantitative difference between these cases is also shown in Table 4.

difficulties would increase, especially at larger flow rates, where timestep sizes under an hour were necessary. Another important issue was regarding the P_c-S_w behaviour in the vicinity and below the gas residual saturation region. A large number of consecutive turning points may be produced by the numerical saturation oscillations in this region, ultimately leading to the scanning curves becoming unbounded. We considered the primary drainage curve for grid blocks starting to fill with gas until their saturation approaches the residual gas saturation to overcome these problems. Moreover, some grid blocks experience substantial gas saturation drops during the H_2 withdrawal. As a result, their saturations approach residual gas, and they may also experience saturation oscillations near this area that can result in unbounded scanning curves. Transferring from the last properly-generated scanning curve to the main drainage curve appeared to be the simplest way to get around this issue.

4. Shortcomings and future work

The main purpose of this study has been to investigate the impact of hysteresis in P_c-S_w functions and injection/withdrawal rates on the efficiency of the UHS operations while ignoring the k_r-S_w hysteresis. The authors are fully aware of the significance of k_r data while simulating the hysteresis. However, the primary goal of this study was to solely consider the impact of P_c-S_w hysteresis as it is largely disregarded in the literature. This provided insights under what conditions complexities of P_c-S_w hysteresis are worth investment for practical industrial scale. Clearly, heterogeneity of the reservoirs and wettability distribution (in depleted reservoirs) are major factors that need to be addressed in future studies. Moreover, higher injection/withdrawal rates (capillary number) result in different k_r curves, and including the dynamic k_r effect can be investigated in future studies.

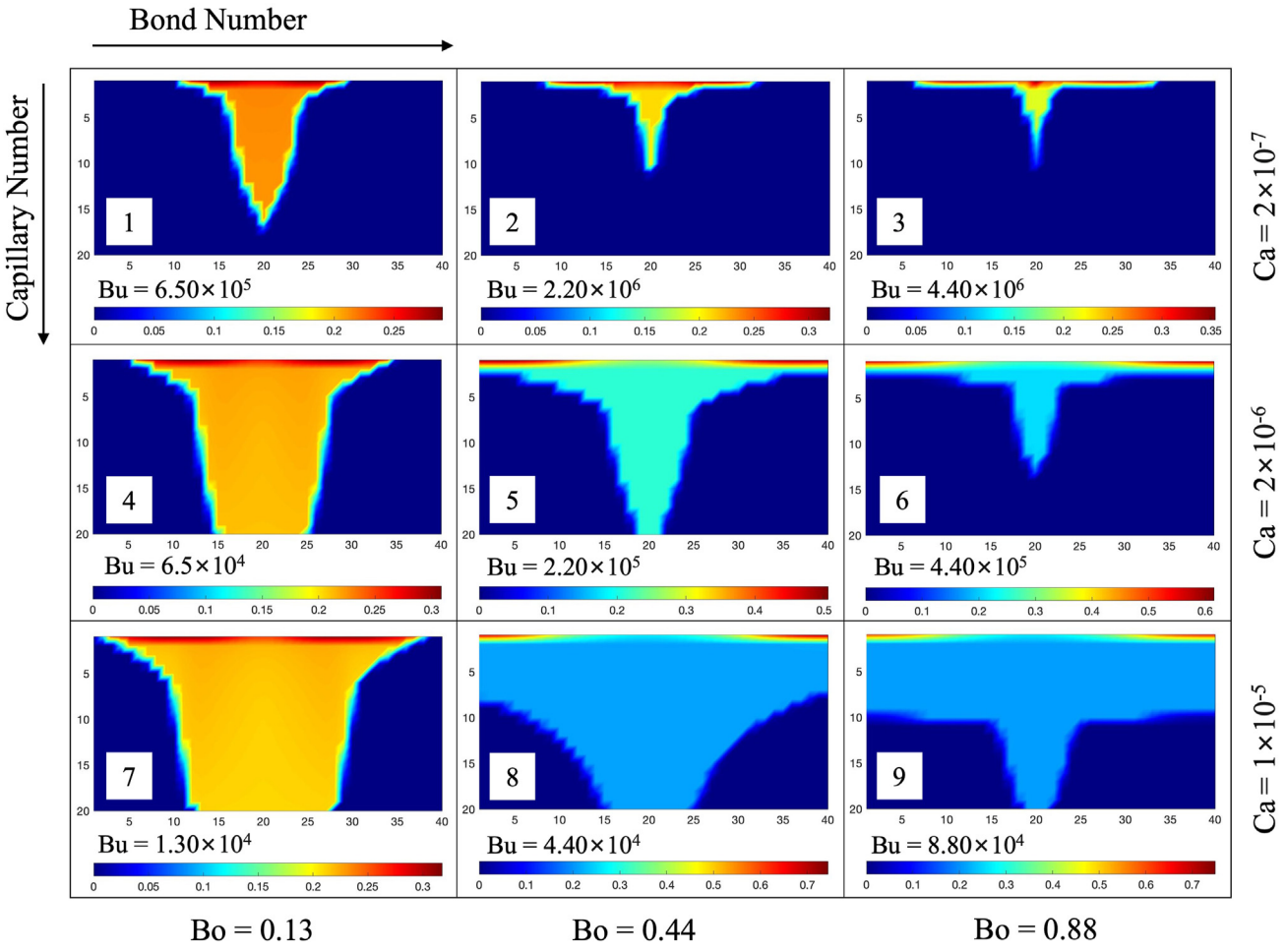

Fig. 8 – Visualisation of hydrogen plume at different capillary, Bond, and Buoyancy numbers at the end of the second withdrawal. Each row presents 3 cases at a constant capillary number. The quantitative difference between these cases is also shown in Table 4.

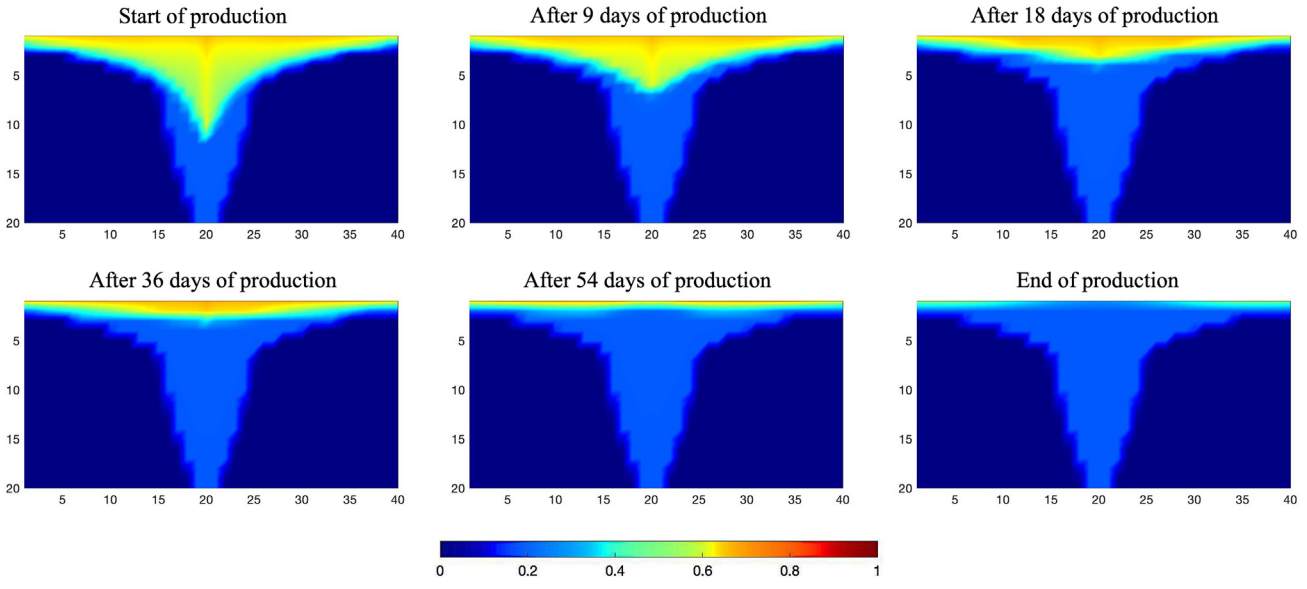

Fig. 9 – An example of the formation of water upconing at six time snapshots during the second cycle of H_2 extraction at rate of 0.13 PV/year ($Bo = 0.44$ and $Ca = 2 \times 10^{-6}$). Beginning with the second withdrawal time and continuing until the time upconing limits the H_2 withdrawal.

5. Conclusions

The inclusion of full hysteretic behaviour of capillary-pressure and relative-permeability functions in two-phase flow simulators impose high computational complexities and are time consuming. Therefore, the first objective of this study was to investigate the sole impact of hysteresis in capillary pressure curves in terms of scanning curve generations, while ignoring the hysteresis in relative permeability. Moreover, this study looked through the effects of operational flow rates and aquifer characteristics in terms of dimensionless parameters (namely capillary number and Bond number) on UHS performance. Analysing the results, the following conclusions are drawn:

- The flow behaviour and effectiveness of the UHS operation were not considerably impacted by the addition of capillary pressure scanning curves in the model. Exclusion of P_c-S_w scanning curves slightly underestimates the remaining hydrogen saturation.
- The impact of capillary pressure on the bottom-hole pressure and withdrawal rate can become significant at late-time withdrawals, when the water is flowing to the well more considerably, and exclusion of capillary pressure clearly overestimates the bottom-hole capillary pressure.
- The UHS efficiency is highly impacted by the operational flow rate, and aquifer characteristics.
- At high capillary numbers, due to the high pressure drop, water bypasses hydrogen and the resulting water upconing ceases the hydrogen withdrawal.
- Aquifer permeability, particularly in the vertical direction, influences the efficiency of UHS. When Bond number presents a small value, gravity segregation is very slow; the interfaces become very diffuse, and the cut-off constraint is satisfied more quickly compared to high permeability scenarios.

Declaration of competing interest

The authors declare that they have no known competing financial interests or personal relationships that could have appeared to influence the work reported in this paper.

Acknowledgements

The authors thank the University of Manchester for funding the PhD studentship of Farzaneh Nazari through the President's Doctoral Scholar Award. The authors thank Prof. Knut Andreas Lie and Dr. Olav Møyner from the SINTEF group for their support via email communications. Rouhi Farajzadeh thanks Shell Global Solutions International B.V., The Hague, Netherlands for granting permission to publish this paper.

Nomenclature

Letters

P_c	Capillary Pressure, Pa
P_e	Entry Capillary Pressure, Pa
k_r	Relative Permeability
k_r^{max}	endpoint relative permeability
n	Brooks-Corey P_c exponent
m	Brooks-Corey k_r exponent
S_w	Water Saturation
S_{rw}	residual Water Saturation
S_w^{max}	maximum attainable wetting-phase saturation
S_w^{Hyst}	wetting-phase turning point saturation
S_g	Gas Saturation
q_g	Gas Velocity, m/s
t^i	Timestep Number
K	Absolute Permeability, m^2
r	Characteristic Pore Radius, m
q	Flow rate, m^3/s
Ca	Capillary Number
Bo	Bond Number
Bu	Buoyancy Number
ϵ	Killough [1] Curvature Parameter
φ	Porosity
μ_g	Gas Viscosity, Pa.s
σ	Interfacial Tension, N/m
θ	Contact Angle, $^\circ$

Abbreviations

UHS	Underground Hydrogen Storage
BC	Brooks-Corey
IFT	Interfacial Tension
AD-OO	Object-Oriented, Automatic-Differentiation
PV	Pore Volume

Appendix A. Sensitivity Analysis

To determine the ideal number of grids for the simulations, a sensitivity analysis regarding the number of grid units is being carried out. Note that the grid aspect ratio is kept constant at 5 in all sensitivity simulations. Figure Appendix A.1 shows the H_2 saturation profiles of four sensitivity analysis cases. To achieve these results, we have considered a single cycle of H_2 injection-withdrawal with rate of 0.015 PV/year. The H_2 was injected for six months and produced for three months after the injection. The results of the sensitivity cases are being compared in terms of an independent parameter, namely the remaining average H_2 saturation. To derive this saturation value, we have considered only the grid blocks which demonstrates H_2 saturation values over 5%. Figure Appendix A.2 presents the error

plot of the conducted sensitivity analysis. The error values are calculated with respect to the point with the lowest number of grids. It can be seen that from the point with 40 × 40 × 20 grids, the average saturation and error values are approaching a plateau. Therefore, we have considered the 40 × 40 × 20 case for the rest of the simulations.

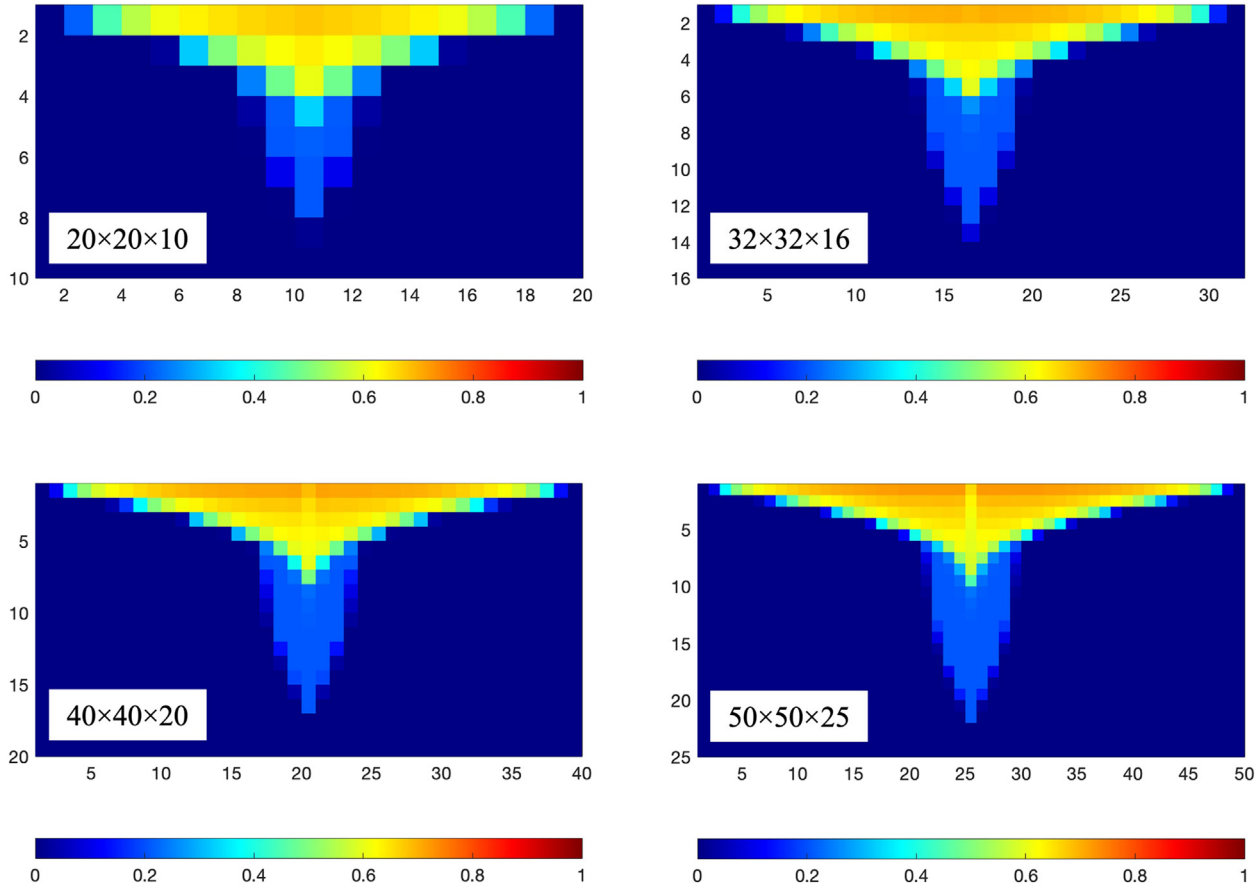

Figure Appendix A.1: The results of sensitivity analysis conducted regarding the number of grids. The grid aspect ratio in all cases is equal 5. The results illustrates the H_2 saturation profile after 6-months injection with rate of 0.015 PV/year. The X and Y axes demonstrate the grid numbers in the corresponding directions.

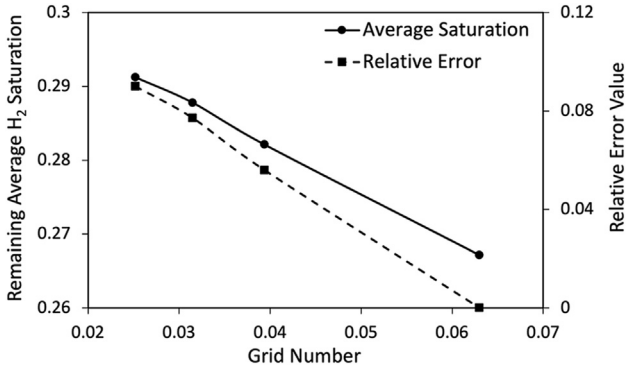

Figure Appendix A.2: The grid sensitivity results as a function of remaining average H_2 saturation ($S_g > 0.05$) after a 3-months withdrawal with rate of 0.015 PV/year. The x-axis demonstrates the grid number derived based on $1/\sqrt[3]{n_x n_y n_z}$. The secondary y-axis also shows the average saturation relative error calculated with respect to the case with lowest number of grids $(|S^i_{g,avg} - S^1_{g,avg}|/S^1_{g,avg})$.

Appendix B. Operational Flow rate and Pressure Plots

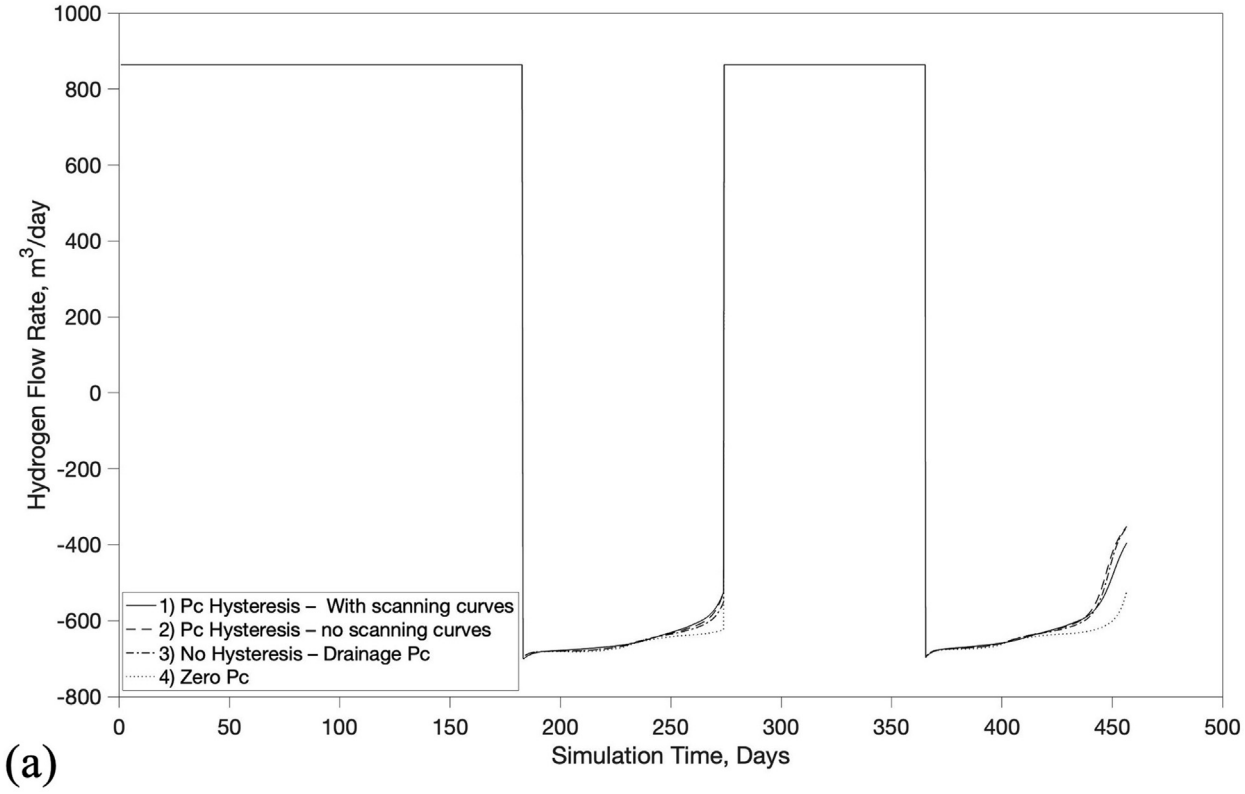

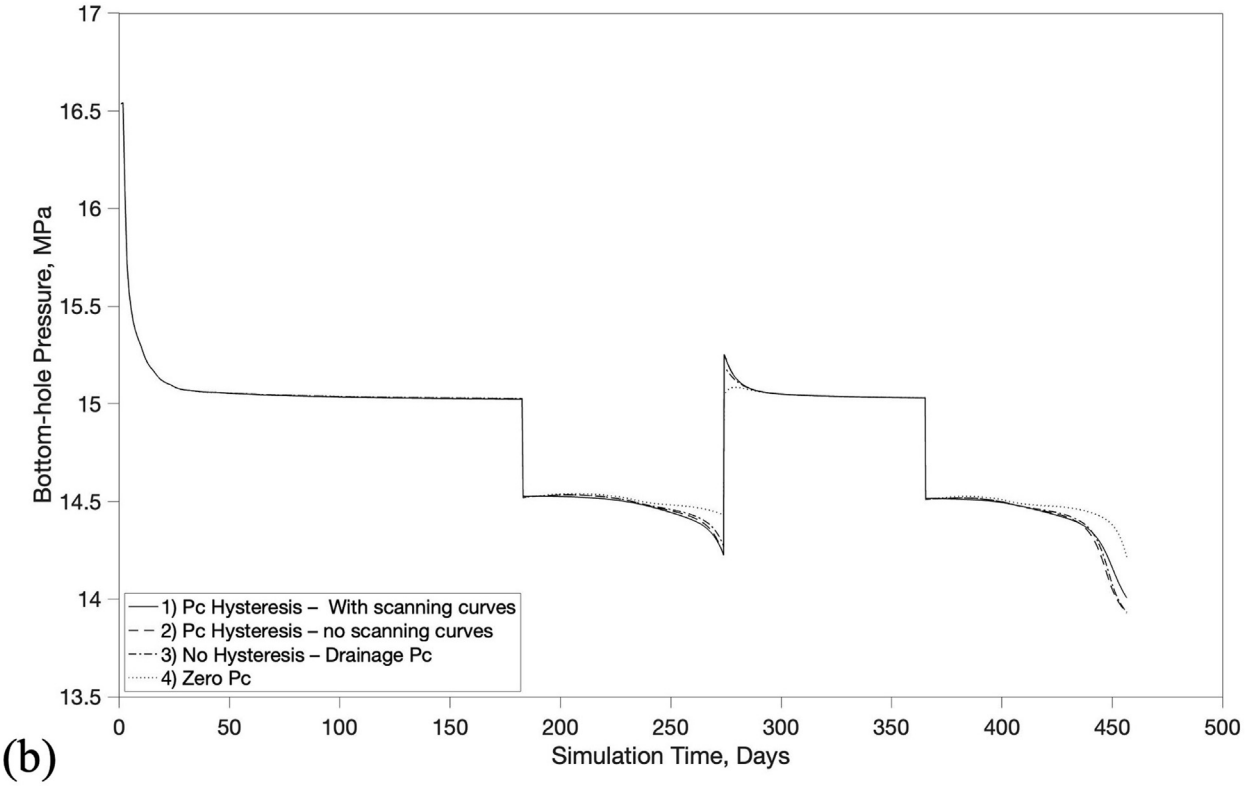

Figure Appendix B.1: H_2 injection/withdrawal rate (a) and bottom-hole pressure (b) versus simulation time for the four hysteresis cases presented in Table 3.

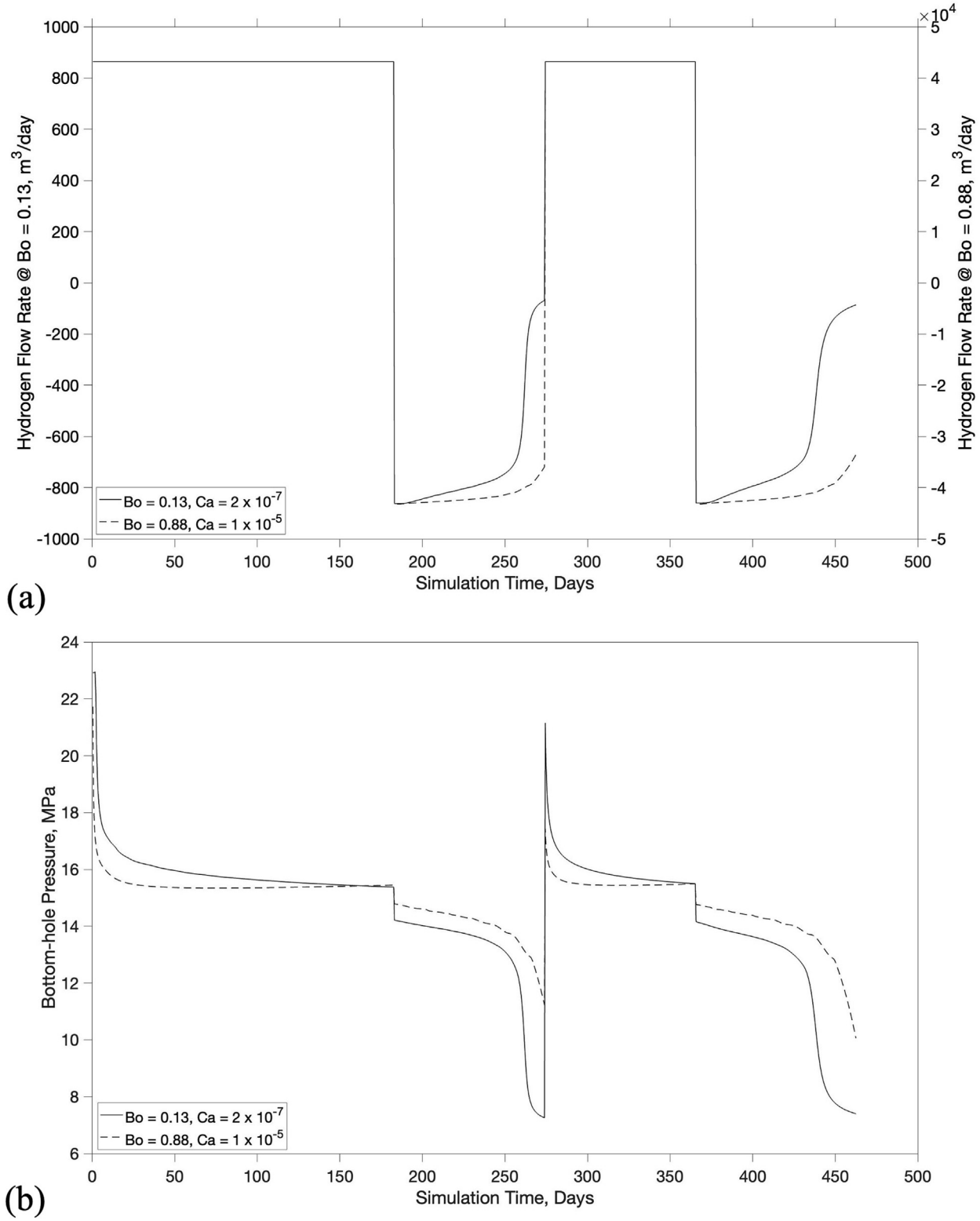

Figure Appendix B.2: H_2 injection/withdrawal rate (a) and bottom-hole pressure (b) versus simulation time for the the two extreme cases (1 and 9) presented in Table 4.

Appendix C. Impact of Gas Compressibility

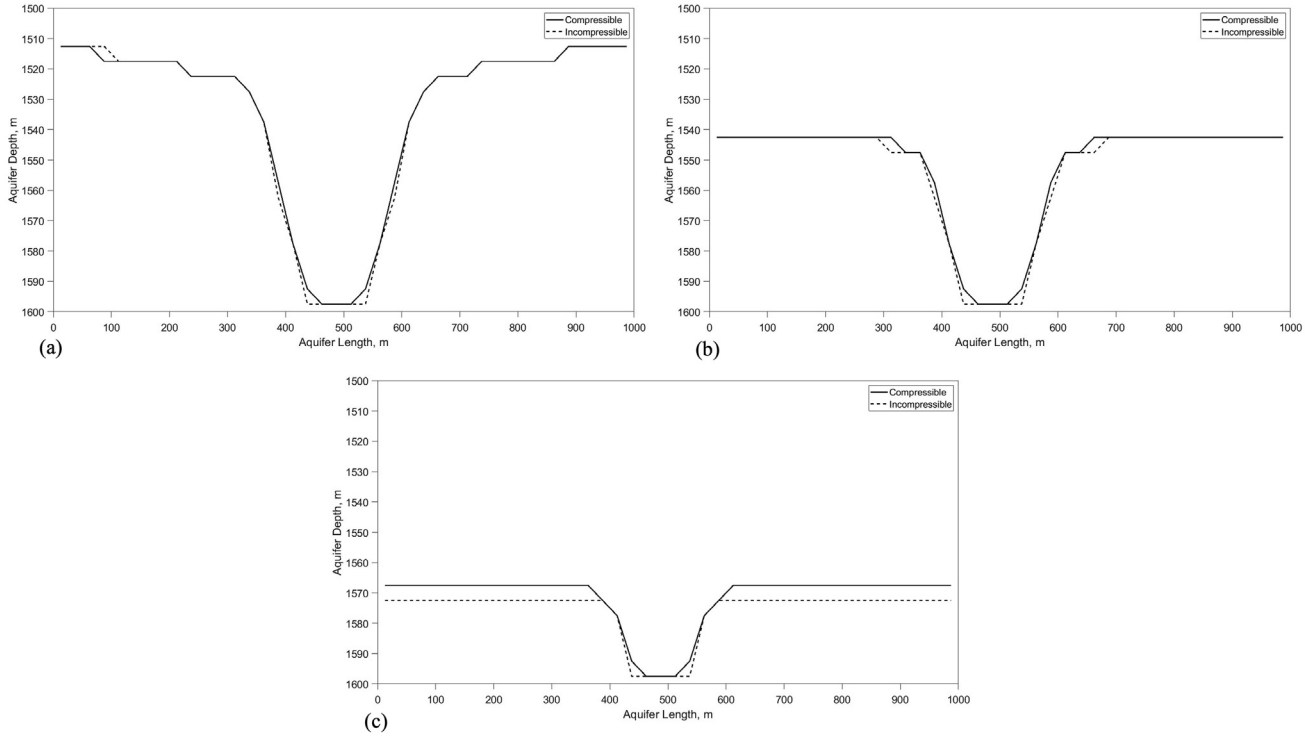

Figure Appendix C.1: H_2 injection front after (a) 0.1, (b) 0.3, and (c) 0.5 total injected pore volume for two compressible and incompressible gas phases. These simulations were done based on the Case 5 data presented in Table 4.

REFERENCES

[1] Killough J. Reservoir simulation with history-dependent saturation functions. Soc Petrol Eng J 1976;16:37–48.
[2] Lie K-A. An introduction to reservoir simulation using MATLAB/GNU Octave: user guide for the MATLAB Reservoir Simulation Toolbox (MRST). Cambridge University Press; 2019.
[3] Heinemann N, Alcalde J, Miocic JM, Hangx SJ, Kallmeyer J, Ostertag-Henning C, Hassanpouryouzband A, Thaysen EM, Strobel GJ, Schmidt-Hattenberger C, et al. Enabling large-scale hydrogen storage in porous media–the scientific challenges. Energy Environ Sci 2021;14:853–64.
[4] Hemme C, Van Berk W. Hydrogeochemical modeling to identify potential risks of underground hydrogen storage in depleted gas fields. Appl Sci 2018;8:2282.
[5] Abe JO, Popoola A, Ajenifuja E, Popoola OM. Hydrogen energy, economy and storage: review and recommendation. Int J Hydrogen Energy 2019;44:15072–86.
[6] Singla MK, Nijhawan P, Oberoi AS. Hydrogen fuel and fuel cell technology for cleaner future: a review. Environ Sci Pollut Control Ser 2021;28:15607–26.
[7] Appleby A. Fuel cells and hydrogen fuel. Int J Hydrogen Energy 1994;19:175–80.
[8] Lototskyy MV, Tolj I, Pickering L, Sita C, Barbir F, Yartys V. The use of metal hydrides in fuel cell applications. Prog Nat Sci: Mater Int 2017;27:3–20.
[9] Yartys V, Zavaliy I, Berezovets V, Pirskyy Y, Manilevich F, Kytsya A, Verbovytskyy Y, Dubov Y, Kutsyi A. Hydrogen generator integrated with fuel cell for portable energy supply. J Phys: Energy 2022;5:014014.
[10] Haseli Y. Maximum conversion efficiency of hydrogen fuel cells. Int J Hydrogen Energy 2018;43:9015–21.
[11] Lin R-H, Xi X-N, Wang P-N, Wu B-D, Tian S-M. Review on hydrogen fuel cell condition monitoring and prediction methods. Int J Hydrogen Energy 2019;44:5488–98.
[12] Zivar D, Kumar S, Foroozesh J. Underground hydrogen storage: a comprehensive review. Int J Hydrogen Energy 2021;46:23436–62.
[13] Tarasov BP, Arbuzov AA, Mozhzhuhin SA, Volodin AA, Fursikov PV, Lototskyy MV, Yartys VA. Hydrogen storage behavior of magnesium catalyzed by nickel-graphene nanocomposites. Int J Hydrogen Energy 2019;44:29212–23.
[14] Pasquini L, Sakaki K, Akiba E, Allendorf MD, Alvares E, Ares JR, Babai D, Baricco M, Von Colbe JB, Bereznitsky M, et al. Magnesium-and intermetallic alloys-based hydrides for energy storage: modelling, synthesis and properties. Progress in energy 2022;4:032007.
[15] Sáinz-García A, Abarca E, Rubí V, Grandia F. Assessment of feasible strategies for seasonal underground hydrogen storage in a saline aquifer. Int J Hydrogen Energy 2017;42:16657–66.
[16] Pan B, Liu K, Ren B, Zhang M, Ju Y, Gu J, Zhang X, Clarkson CR, Edlmann K, Zhu W, et al. Impacts of relative permeability hysteresis, wettability, and injection/withdrawal schemes on underground hydrogen storage in saline aquifers. Fuel 2023;333:126516.
[17] Bo Z, Boon M, Hajibeygi H, Hurter S. Impact of experimentally measured relative permeability hysteresis on

reservoir-scale performance of underground hydrogen storage (uhs). Int J Hydrogen Energy 2023;48(36):13527–42.
[18] Amid A, Mignard D, Wilkinson M. Seasonal storage of hydrogen in a depleted natural gas reservoir. Int J Hydrogen Energy 2016;41:5549–58.
[19] Ozarslan A. Large-scale hydrogen energy storage in salt caverns. Int J Hydrogen Energy 2012;37:14265–77.
[20] Caglayan DG, Weber N, Heinrichs HU, Linßen J, Robinius M, Kukla PA, Stolten D. Technical potential of salt caverns for hydrogen storage in europe. Int J Hydrogen Energy 2020;45:6793–805.
[21] Dopffel N, Jansen S, Gerritse J. Microbial side effects of underground hydrogen storage–knowledge gaps, risks and opportunities for successful implementation. Int J Hydrogen Energy 2021;46:8594–606.
[22] Chen Y, Niasar V, Ma L, Xie Q. Effect of salinity, mineralogy, and organic materials in hydrogen wetting and its implications for underground hydrogen storage (uhs). Int J Hydrogen Energy 2023. https://doi.org/10.1016/j.ijhydene.2023.05.085. URL: https://www.sciencedirect.com/science/article/pii/S0360319923023376.
[23] Pfeiffer WT, Bauer S. Subsurface porous media hydrogen storage–scenario development and simulation. Energy Proc 2015;76:565–72.
[24] Pfeiffer W, Al Hagrey S, Köhn D, Rabbel W, Bauer S. Porous media hydrogen storage at a synthetic, heterogeneous field site: numerical simulation of storage operation and geophysical monitoring. Environ Earth Sci 2016;75:1–18.
[25] Feldmann F, Hagemann B, Ganzer L, Panfilov M. Numerical simulation of hydrodynamic and gas mixing processes in underground hydrogen storages. Environ Earth Sci 2016;75:1–15.
[26] Hagemann B, Rasoulzadeh M, Panfilov M, Ganzer L, Reitenbach V. Mathematical modeling of unstable transport in underground hydrogen storage. Environ Earth Sci 2015;73:6891–8.
[27] Hagemann B, Rasoulzadeh M, Panfilov M, Ganzer L, Reitenbach V. Hydrogenization of underground storage of natural gas. Comput Geosci 2016;20:595–606.
[28] Rubin E, De Coninck H. Ipcc special report on carbon dioxide capture and storagevol. 2. UK: Cambridge University Press. TNO; 2004. p. 14. Cost Curves for CO2 Storage, Part.
[29] Joekar-Niasar V, Doster F, Armstrong R, Wildenschild D, Celia MA. Trapping and hysteresis in two-phase flow in porous media: a pore-network study. Water Resour Res 2013;49:4244–56.
[30] Wang Y, Vuik C, Hajibeygi H. Analysis of hydrodynamic trapping interactions during full-cycle injection and migration of co2 in deep saline aquifers. Adv Water Resour 2022;159:104073.
[31] Juanes R, Spiteri E, Orr Jr F, Blunt M. Impact of relative permeability hysteresis on geological co2 storage. Water Resour Res 2006;42.
[32] Carlson FM. Simulation of relative permeability hysteresis to the nonwetting phase. In: SPE annual technical conference and exhibition. OnePetro; 1981.
[33] Kleppe J, Delaplace P, Lenormand R, Hamon G, Chaput E. Representation of capillary pressure hysteresis in reservoir simulation. In: SPE annual technical conference and exhibition. OnePetro; 1997.
[34] Tan T. Representation of hysteresis in capillary pressure for reservoir simulation models. J Can Petrol Technol 1990;29.
[35] Land CS. Calculation of imbibition relative permeability for two-and three-phase flow from rock properties. Soc Petrol Eng J 1968;8:149–56.
[36] Larsen J, Skauge A. Methodology for numerical simulation with cycle-dependent relative permeabilities. SPE J 1998;3:163–73.
[37] Spiteri EJ, Juanes R, Blunt MJ, Orr FM. A new model of trapping and relative permeability hysteresis for all wettability characteristics. SPE J 2008;13:277–88.
[38] Steffy D, Barry D, Johnston C. Influence of antecedent moisture content on residual lnapl saturation. Soil Sediment Contam 1997;6:113–47.
[39] Mualem Y. A conceptual model of hysteresis. Water Resour Res 1974;10:514–20.
[40] Aghabozorgi S, Sohrabi M. A comparative study of predictive models for imbibition relative permeability and trapped non-wetting phase saturation. J Nat Gas Sci Eng 2018;52:325–33.
[41] Aghabozorgi S, Sohrabi M. Generalised model for simulation of two-and three-phase cycle-dependent hysteresis in sandstones. Fuel 2022;310:122328.
[42] Akbarabadi M, Piri M. Relative permeability hysteresis and capillary trapping characteristics of supercritical co2/brine systems: an experimental study at reservoir conditions. Adv Water Resour 2013;52:190–206.
[43] Zulfiqar B, Vogel H, Ding Y, Golmohammadi S, Küchler M, Reuter D, Geistlinger H. The impact of wettability and surface roughness on fluid displacement and capillary trapping in 2-d and 3-d porous media: 2. combined effect of wettability, surface roughness, and pore space structure on trapping efficiency in sand packs and micromodels. Water Resour Res 2020;56:e2020WR027965.
[44] Spiteri E, Juanes R, Blunt MJ, Orr FM. Relative permeability hysteresis: trapping models and application to geological co2 sequestration. In: SPE annual technical conference and exhibition. OnePetro; 2005.
[45] Ide ST, Jessen K, Orr Jr FM. Storage of co2 in saline aquifers: effects of gravity, viscous, and capillary forces on amount and timing of trapping. Int J Greenh Gas Control 2007;1:481–91.
[46] Gershenzon NI, Ritzi Jr RW, Dominic DF, Mehnert E, Okwen RT. Capillary trapping of co2 in heterogeneous reservoirs during the injection period. Int J Greenh Gas Control 2017;59:13–23.
[47] Gershenzon NI, Soltanian M, Ritzi Jr RW, Dominic DF. Co2 capillary-trapping processes in deep saline aquifers. In: EGU general assembly conference abstracts; 2014. p. 3935.
[48] Gershenzon NI, Soltanian M, Ritzi Jr RW, Dominic DF. Influence of small scale heterogeneity on co2 trapping processes in deep saline aquifers. Energy Proc 2014;59:166–73.
[49] Gershenzon NI, Ritzi Jr RW, Dominic DF, Soltanian M, Mehnert E, Okwen RT. Influence of small-scale fluvial architecture on co2 trapping processes in deep brine reservoirs. Water Resour Res 2015;51:8240–56.
[50] Yang Z, Chen Y-F, Niemi A. Gas migration and residual trapping in bimodal heterogeneous media during geological storage of co2. Adv Water Resour 2020;142:103608.
[51] Boon M, Hajibeygi H. Experimental characterization of h 2/water multiphase flow in heterogeneous sandstone rock at the core scale relevant for underground hydrogen storage (uhs). Sci Rep 2022;12:14604.
[52] Group CM. User's guide gem, advanced compositional reservoir simulator. Computer Modeling Group; 2020.
[53] Lysyy M, Fernø MA, Ersland G. Effect of relative permeability hysteresis on reservoir simulation of underground hydrogen storage in an offshore aquifer. J Energy Storage 2023;64:107229.
[54] Lysyy M, Føyen T, Johannesen EB, Fernø M, Ersland G. Hydrogen relative permeability hysteresis in underground storage. Geophys Res Lett 2022;49:e2022GL100364.
[55] Lie K-A, Møyner O. Advanced modelling with the MATLAB reservoir simulation toolbox. Cambridge University Press; 2021.

[56] Nazari F, Farajzadeh R, Niasar VJ. Critical parameters controlling wettability in hydrogen underground storage-an analytical study. JCIS Open 2022;8:100063.
[57] Plug W-J, Bruining J. Capillary pressure for the sand–co2–water system under various pressure conditions. application to co2 sequestration. Adv Water Resour 2007;30:2339–53.
[58] Leverett M. Capillary behavior in porous solids. Transactions of the AIME 1941;142:152–69.
[59] Brooks RH, Corey AT. Properties of porous media affecting fluid flow. J Irrigat Drain Div 1966;92:61–88.
[60] Guo Y. Importance of capillary hysteresis on coreflood experiments. In: IOR 1995-8th European symposium on improved oil recovery. EAGE Publications BV; 1995. p. 107.
[61] Debbabi Y, Jackson MD, Hampson GJ, Salinas P. Impact of the buoyancy–viscous force balance on two-phase flow in layered porous media. Transport Porous Media 2018;124:263–87.
[62] Shook M, Li D, Lake LW. Scaling immiscible flow through permeable media by inspectional analysis, In Situ;(United States)vol. 16; 1992.
[63] Francke H, Thorade M. Density and viscosity of brine: an overview from a process engineers perspective. Geochemistry 2010;70:23–32.
[64] Hilsenrath J, Touloukian Y. The viscosity, thermal conductivity, and Prandtl number for air, o2, n2, no, h2, co, co2, h2o, he, and a. Trans Am Soc Mech Eng 1954;76:967–83.
[65] Sari A, Al Maskari NS, Saeedi A, Xie Q. Impact of surface roughness on wettability of oil-brine-calcite system at sub-pore scale. J Mol Liq 2020;299:112107.
[66] Chow YF, Maitland GC, Trusler JM. Interfacial tensions of the (co2+ n2+ h2o) system at temperatures of (298 to 448) k and pressures up to 40 mpa. J Chem Therm 2016;93:392–403.
[67] Lenhard R, Parker J, Mishra S. On the correspondence between brooks-corey and van genuchten models. J Irrigat Drain Eng 1989;115:744–51.
[68] Kashif M, Cao Y, Yuan G, Asif M, Javed K, Mendez JN, Khan D, Miruo L. Pore size distribution, their geometry and connectivity in deeply buried paleogene es1 sandstone reservoir, nanpu sag, east China. Petrol Sci 2019;16:981–1000.